The Astrophysical Journal, 916:57 (8pp), 2021 July 20 https://doi.org/10.3847/1538-4357/ac05b7


# Boundary Conditions at the Heliospheric Termination Shock with Pickup Ions

Michael Gedalin[1], Nikolai V. Pogorelov[2,3], and Vadim Roytershteyn[4]
[1] Department of Physics, Ben Gurion University of the Negev, Beer-Sheva, Israel; gedalin@bgu.ac.il
[2] Department of Space Science, The University of Alabama in Huntsville, AL 35805, USA
[3] Center for Space Plasma and Aeronomic Research, The University of Alabama in Huntsville, AL 35805, USA
[4] Space Science Institute, Boulder, CO 80301, USA
*Received 2021 March 25; revised 2021 May 25; accepted 2021 May 25; published 2021 July 27*

## Abstract

In a collisionless shock the directed flow energy is converted mainly in thermal energy of the plasma species. At the termination shock (TS) a substantial portion of energy goes into heating of pickup ions (PUIs), while heating of the solar wind protons (SW) is weaker than it would be without PUI. Heating of both species is nonadiabatic. Downstream pressure of the mixture is determined by conservation laws for the whole mixture. SW heating is sensitive to the details of the shock front, while heating of PUI is not. The profile is an analytical approximation of the observed TS. Here the downstream temperature and pressure of PUIs are obtained for the first time using test particle analysis in a model shock profile for various magnetic compression ratios and shock angles. The profile is an analytical approximation of the observed TS. The results of the analysis are used in the pressure balance equation and the corresponding SW heating is estimated. The analysis is supported by full particle simulations, except for the SW heating that was not studied using test particle data due to its apparent dependence on fine structure of the shock front.

*Unified Astronomy Thesaurus concepts:* Shocks (2086); Termination shock (1690); Interplanetary shocks (829); Heliosphere (711)

## 1. Introduction

Collisionless shocks are one of the most ubiquitous phenomena in space plasmas. The directed flow energy is converted into other forms at the shock front: ion and electron heating, particle acceleration, and magnetic field enhancement. One of the most important problems of the collisionless shock physics is prediction of the post-shock (downstream) state of the plasma and fields given the corresponding plasma and magnetic field state before the shock (upstream). In the absence of dissipative processes the relations between the upstream and downstream parameters (Rankine–Hugoniot relations, boundary conditions, and jump conditions) are just conservation laws of particle number, momentum, and energy. There is a complete hierarchy of scales in collisionless shocks and, accordingly, the boundary conditions depend on the scale at which the boundaries are placed. The standard Rankine–Hugoniot relations (RH) are formulated on the largest, magnetohydrodynamic (MHD) scale, at which the distributions thermalize (Kennel 1994). In many space plasma environments the ambient conditions change on spatial or temporal scales, which are too short to achieve such thermalization. Observational comparison of the upstream and downstream plasma is often done in various regions that do not satisfy the conditions for establishing the MHD RH. In the close vicinity of the shock front, ion distributions are significantly gyrophase dependent, and the jump conditions at the very transition should take this into account (Gedalin & Balikhin 2008; Gedalin 2016a). On larger scales or for measurements invoking substantial temporal and/or spatial averaging, the distributions become gyrotropic but can still remain anisotropic, since isotropization may be slow. The corresponding RH should take into account this anisotropy (Lyu & Kan 1986; Gedalin 2017; Gedalin et al. 2020). Additional complications arise when there are different populations of ions that undergo gyrotropization and isotropization on different scales. Eventual equilibration of temperatures may never happen. Even for different populations of ions of the same kind eventual merging into one thermal population may never be observed. The latter situation is expected to be typical when pickup ions (PUIs) are important constituents, as at the termination shock (Zank et al. 1996; Li et al. 2008; Richardson et al. 2008; Burrows et al. 2010; Matsukiyo & Scholer 2011, 2014; Ariad & Gedalin 2013; Jokipii 2013; Mostafavi et al. 2017, 2018; Kumar et al. 2018). In this case, MHD has to be replaced with a multispecies model, where each population obeys the corresponding conservation laws separately, while the magnetic field jump is obtained by combining all species together. In this approach one has to know the equations of state for each species. Typically, some form of thermodynamics motivated state equations are assumed (Florinski et al. 2009; Borovikov et al. 2011; Pogorelov et al. 2013; Zank et al. 2014; Mostafavi et al. 2018). This approach implicitly assumes that the population is in a kind of local thermodynamic equilibrium. However, observations show that this is not the case. In fact, the downstream ion distribution is determined primarily by ion dynamics in the macroscopic fields of the shock front. Interaction with the electromagnetic fluctuations plays a secondary role causing slow relaxation toward equilibrium, while binary collisions are negligible. The resolution of particle observations in the vicinity of the heliospheric termination shock corresponds to the scale on which the solar wind protons are possibly (but not certainly) isotropic but PUI are still anisotropic. Yet most studies of RH at the termination shock aim at the determination of jump conditions on the MHD scale, assuming isotropy of the distributions. Some previous analyses within a two-fluid model (solar wind and PUI) introduced heat flux and collisionless viscosity of PUI (Zank et al. 2014; Mostafavi et al. 2016, 2017, 2018; Zank 2016). This approach explicitly assumes that ion scattering within the shock transition is substantial so that the focused transport equation is valid throughout the shock (Zank et al. 2014). However, the shock transition is scatter-free (Toptyghin 1980; Drury 1983), so that the approach loses the physics of relation between the kinetic and

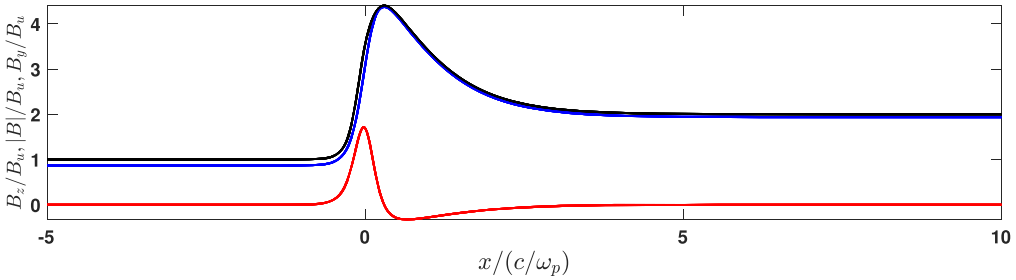


**Figure 1.** The magnetic profile used in the analysis, $|\boldsymbol{B}|$ (black), $B_z$ (blue), and $B_y$ (red).

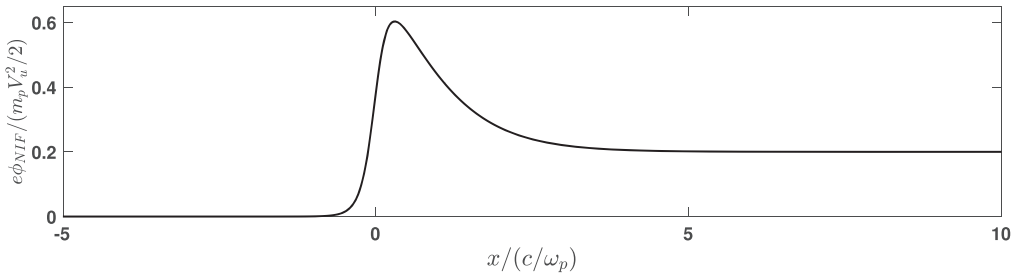


**Figure 2.** The cross-shock potential used in the analysis.

MHD scales. Accordingly, the obtained magnetic profiles are monotonic and cannot explain observed overshoots (Mostafavi et al. 2018). Previous attempts to take into account the ion kinetics at a shock front assumed magnetic moment conservation (Fahr & Chalov 2008; Fahr et al. 2012; Fahr & Siewert 2013, 2015). However, it has been shown that magnetic moment is, in general, not conserved (Terasawa 1979; Gedalin 2020), and such approximation may be satisfactory only in the perpendicular regime. Proper establishment of the boundary conditions on MHD scales requires establishing a relation of the ultimately isotropic distributions to the collisionless ion dynamics within a shock front. This objective requires proper determination of downstream gyrophase averaged distributions, which are gyrotropic but anisotropic, with further relating these to the isotropic pressure (Gedalin et al. 2020). In the present paper, we numerically determine the parameters of these distributions, which will be used for modifying the Rankine–Hugoniot relation.

## 2. Basic Setup

Since ion dynamics inside the shock front is nonadiabatic and the equations of motion are not integrable, the analysis will be performed numerically, by tracing ions in the electric and magnetic fields of a model shock profile. In the present paper we restrict ourselves by the consideration of a stationary and one-dimensional profiles, leaving the analysis of time-dependence and nonplanarity for further studies. The main features, ramp and overshoot, of the shock profile chosen for our analysis are taken to be generally similar to the observed termination shock (Burlaga et al. 2008; Richardson et al. 2008). The main component of the magnetic field $B_z$ is modeled using the asymmetric overshoot profile

$$B_1 = \left(\frac{R+1}{2}\right) + \left(\frac{R-1}{2}\right)\tanh\left(\frac{ax}{D}\right) \tag{1}$$

$$f_l = \frac{1}{2}\left[1 + \tanh\left(\frac{x - C_l}{W_l}\right)\right] \tag{2}$$

$$f_r = \frac{1}{2}\left[1 - \tanh\left(\frac{x - C_r}{W_r}\right)\right] \tag{3}$$

$$B_z = (B_1 + B_o f_1 f_2) B_u \sin\theta_u \tag{4}$$

$$\frac{B_d}{B_u} = \sqrt{R^2\sin^2\theta_u + \cos^2\theta_u}. \tag{5}$$

Here $\theta_u$ is the angle between the shock normal and the upstream magnetic field vector, $x$ is the coordinate along the normal directed toward upstream, $x$–$z$ is the shock coplanarity plane, $B_u$ and $B_d$ are the upstream and downstream magnitudes of the magnetic fields, respectively, $R$ is the ratio of the downstream and upstream $z$ components of the magnetic field, and the rest of the parameters are adjusted so that a profile in Figure 1 is obtained. The cross-shock electric field $E_x$ and noncoplanar magnetic field $B_y$ are modeled using $B_y \propto E_x \propto dB_z/dx$, so that the de Hoffman–Teller cross-shock potential $\phi_{\rm HT} = -\int E_x dx$ and the Normal Incidence Frame (NIF) cross-shock potential

$$\phi_{\rm NIF} = \phi_{\rm HT} + (V_u \tan\theta_u/c)\int B_y dx \tag{6}$$

are variable model parameters. Ion tracing is performed in the de Hoffman–Teller frame (HT), where the upstream plasma flow is along the magnetic field, $\boldsymbol{V}_{{\rm HT},u} = (V_u, 0, V_u\tan\theta_u)$, and there is no motional electric field, $E_y = E_z = 0$. NIF is the frame in which the upstream plasma flow is along the shock normal. The magnetic compression $B_d/B_u$ and the shock angle $\theta_u$ were varied in the intervals $1.6 \leqslant B_d/B_u \leqslant 2.7$ and $57.^\circ5 \leqslant \theta_u \leqslant 87.^\circ5$. The overshoot amplitude was chosen so that $\max(B_z)/B_{zd} = 2.25$. Here $B_{zd}$ is the $z$-component of the magnetic field in the downstream region far beyond the overshoot. The cross-shock potential was chosen as $\phi_{\rm HT} = 0.1(m_pV_u^2/2)$ and $\phi_{\rm NIF} = 0.2(m_pV_u^2/2)$. Here $V_u$ is the upstream velocity of the plasma flow along the shock normal. In the numerical analysis $V_u/c = 10^{-3}$, where $c$ is the speed of light. Figure 2 shows the cross-shock potential as a function of the coordinate along the

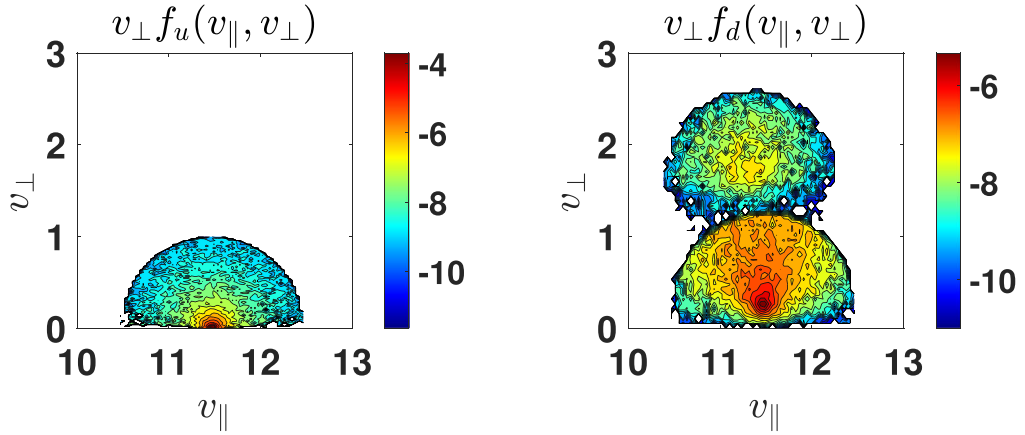


**Figure 3.** The upstream (left) and downstream (right) distributions of PUI for $B_d/B_u = 2.7$ and $\theta_u = 85°$. The colorbar values indicate $\ln[v_\perp f(v_\parallel, v_\perp)]$. See normalization in the text.

shock normal. The potential is zero far upstream of the ramp. The maximum potential is $\phi_{\max} = \phi_{\rm NIF}(\max(B_z)/B_{zd}) \approx 0.45$. The Afvénic shock Mach $M = V_u/v_{\rm A} = 7$ for all runs. Here Alfvén speed is defined as follows: $v_{\rm A}^2 = B_u^2/4\pi n_p m_p$, where $n_p$ is the upstream density of solar wind protons, not including PUI. The ramp width is chosen as $D = (c/\omega_p)$, where $\omega_p^2 = 4\pi n_p e^2/m_p$. In each run, 40,000 PUI were traced across the shock. The upstream distribution PUIs is chosen in the form of a filled shell (Vasyliunas & Siscoe 1976), i.e., $f_u(\boldsymbol{u}) \propto u^{-3/2} H(u_c - u)$, where $u = \sqrt{(v_x - V_u)^2 + v_y^2 + (v_z - V_u \tan\theta_u)^2}$ is the velocity of PUIs in the solar wind frame, $u_c$ is the cutoff speed, and $H$ is the Heaviside step function. The initial distribution already has the form $f_u(v_\parallel, v_\perp)$, independent of gyrophase. Upon crossing the shock, in the quiet downstream region, each ion has certain $(v_\parallel, v_\perp)$, which do not change with distance from the shock, in contrast with the gyrophase, which is position dependent. Therefore, it is sufficient to numerically determine $(v_\parallel, v_\perp)$ for each PUI at some $x > 0$, where the fields are already constant, in order to construct the corresponding downstream $f_d(v_\parallel, v_\perp)$. These distribution functions are used to derive the following moments:

$$n = \int f(v_\parallel, v_\perp) v_\perp dv_\perp dv_\parallel \tag{7}$$

$$nV_\parallel = \int v_\parallel f(v_\parallel, v_\perp) v_\perp dv_\perp dv_\parallel \tag{8}$$

$$P_\parallel = m_p \int (v_\parallel - V_\parallel)^2 f(v_\parallel, v_\perp) v_\perp dv_\perp dv_\parallel \tag{9}$$

$$P_\perp = \frac{1}{2} m_p \int v_\perp^2 f(v_\parallel, v_\perp) v_\perp dv_\perp dv_\parallel. \tag{10}$$

Boundary conditions require the $xx$ component of the total pressure

$$P_{xx} = P_\perp + (P_\parallel - P_\perp)\cos^2\theta + nm_p V_\parallel^2 \cos^2\theta, \tag{11}$$

which includes both kinetic and dynamic pressures. The above expression is valid both upstream and downstream.

## 3. Ion Distributions

Figure 3 illustrates the upstream and downstream distributions of PUI for $B_d/B_u = 2.7$ and $\theta_u = 85°$. In order to better represent the contribution of large $v_\perp$, the distributions are shown as contour plots of $\ln[v_\perp f(v_\parallel, v_\perp)]$, with the normalization $\int v_\perp f(v_\parallel, v_\perp) dv_\perp dv_\parallel = 1$. The downstream distribution consists of two clearly separated populations of PUIs, which are directly transmitted (index $t$ hereinafter) and those that are reflected (index $r$ hereafter) once and proceed further downstream afterwards (Gedalin 1996, 2016b; Lee et al. 1996; Zank et al. 1996, 2010; Zilbersher & Gedalin 1997). The latter have larger $v_\perp$. In what follows, all parameters refer to PUI and normalized variables are used: velocities are normalized to the upstream plasma velocity along the shock normal $V_u$, densities are normalized to the upstream density of PUI $n_u$, pressures are normalized to $n_u m_p V_u^2$, and temperatures are normalized to $m_p V_u^2$. The normalized upstream temperature of PUI is then $T_u = 0.14$. In this run $n_d = 2.71$, $P_{d,\perp} = 1.79$, and $P_{d,xx} = 2.16$. Separate treatment of transmitted and reflected populations has been proposed for boundary conditions (Zank et al. 2010). It was suggested (Lee et al. 1996; Zank et al. 1996, 2010) that it is those ions that satisfy the condition $m_p v_x^2/2 < e\phi_{\max}$ that are reflected. In this run, transmitted and reflected ions are separated by $v_\perp = 1.23$. The expected percentage of the ions reflected by the cross-shock potential (Zank et al. 2010) for our model shock is 15%, while the direct numerical ion tracing shows that 22% of PUI are reflected. This means that reflection is not determined by the potential alone and gyration in the magnetic field is essential. Accordingly, $n_r = 0.72$, i.e., about 26% of the downstream PUI density belongs to PUI, which have been reflected once. The pressure of the reflected PUI is $P_{r,\perp} = 1.31$, which constitutes almost 0.75 of the perpendicular downstream pressure of PUI. The ratio $P_{r,xx}/P_{d,xx} = 0.65$. The total downstream perpendicular temperature is $T_{d,\perp} = 0.65$, and the temperature ratio is $T_{d,\perp}/T_u = 4.65$, in agreement with the previously found heating (Gedalin et al. 2020). This heating is substantially stronger than the one predicted by magnetic moment conservation (Fahr & Chalov 2008). Transmitted and reflected ions are heated differently. For reflected ions alone $T_{r,\perp}/T_u = 12.85$ and $T_{r,\perp} = 1.8$. The downstream temperature of reflected ions as predicted by Equation (10) of Zank et al. (2010) is $T_{r,\perp} \approx 22.5$, by an order of magnitude larger than found in the present analysis. Figure 4 shows the downstream distribution of PUIs for several combinations of the magnetic compression and angle. For lower angles, there appears a weak third population that corresponds to doubly reflected PUI, which is more pronounced for higher magnetic compressions. In general, the population of reflected ions is stronger for larger $B_d/B_u$. Note that the maximum cross-shock potential $\phi_{\max}$ in the numerical analysis depends only

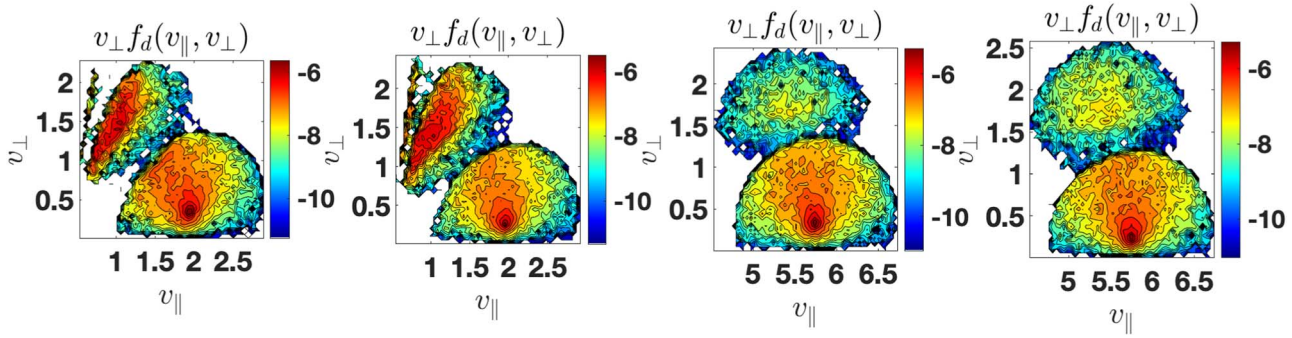


**Figure 4.** The downstream distributions of PUI for several combinations of the magnetic compression and angle. From left to right: (a) $B_d/B_u = 2.2$ and $\theta_u = 60°$, (b) $B_d/B_u = 2.6$ and $\theta_u = 60°$, (c) $B_d/B_u = 2.2$ and $\theta_u = 80°$, and (d) $B_d/B_u = 2.6$ and $\theta_u = 80°$. The colorbar values indicate $\ln[v_\perp f(v_\parallel, v_\perp)]$. See normalization in the text.

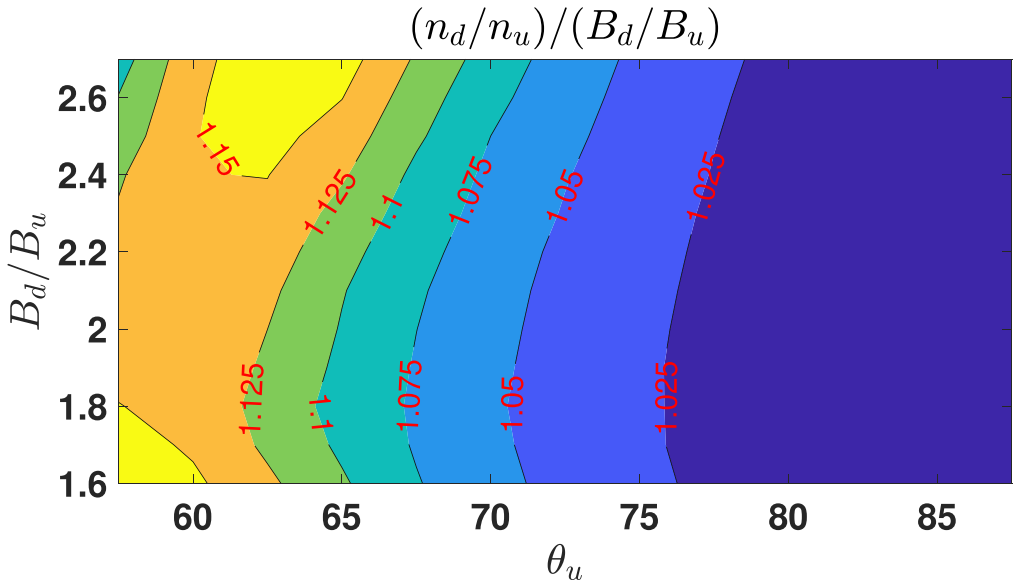


**Figure 5.** Ratio of density compression to magnetic compression $(n_d/n_u)/(B_d/B_u)$.

weakly on the magnetic compression and angle. It is smaller for higher $B_d/B_u$ for the same $\theta_u$. This observation supports the above conclusion that the cross-shock potential is not the only and probably not the main parameter that determines the intensity of PUI reflection.

Figure 5 shows the ratio of the density compression to the magnetic compression $(n_d/n_u)/(B_d/B_u)$. This ratio varies in the range 1–1.17. Deviation from unity is stronger for lower angles. For applications with boundary conditions one can use the approximation $n_d/n_u = B_d/B_u$.

Besides the density compression, we are interested in the perpendicular heating $T_{d,\perp}/T_u$ (parallel heating is negligible) and total $P_{d,xx}$.

Figure 6 shows the perpendicular heating $T_{d,\perp}/T_u$ as a function of $B_d/B_u$ and $\theta_u$. Figure 7 shows the dependence of the perpendicular heating $T_{d,\perp}/T_u$ as a function of $B_d/B_u$ for various $\theta_u$. For $B_d/B_u > 2$ the relation is approximately linear:

$$\frac{T_{d,\perp}}{T_u} \approx 1.75\frac{B_d}{B_u}, \tag{12}$$

with only weak dependence on the shock angle, as can be seen in Figure 8, which shows the dependence of the perpendicular heating $T_{d,\perp}/T_u$ as a function of $\theta_u$ for various $B_d/B_u$. For larger angles, heating is stronger for larger magnetic compressions.

Figure 9 shows the dependence of $P_{d,xx}$ on $B_d/B_u$ and $\theta_u$. The dependence on $B_d/B_u$ for various $\theta_u$ is shown in Figure 10 while the dependence on $\theta_u$ for various $B_d/B_u$ is shown in Figure 11. The dependence on the angle for $\theta_u > 65°$ is weak. A numerically fitted dependence is

$$P_{d,xx} = P_0 + \left[\left(\frac{B_d}{B_u}\right)^2 - r_0\right] \quad \text{for} \quad B_d/B_u > 1.8, \tag{13}$$

where $r_0 = 1.8^2$ and $P_0 = 1.4$, while $P_{d,xx} = P_0$ for $B_d/B_u < 1.8$. At this stage we have no analytical support for this fit.

Mach number affects ion heating only indirectly, via the shock structure, which is Mach dependent. For given magnetic compression, overshoot strength, and shock angle, the Alfvén Mach number is a parameter that does not enter any dependencies. In order to study the dependence of the heating on the Mach number one has to know the dependence of $B_d/B_u$ and $\max(B_z)/B_{zd}$ on the shock angle and Mach number. At this stage no good theory exists that could provide us with this knowledge.

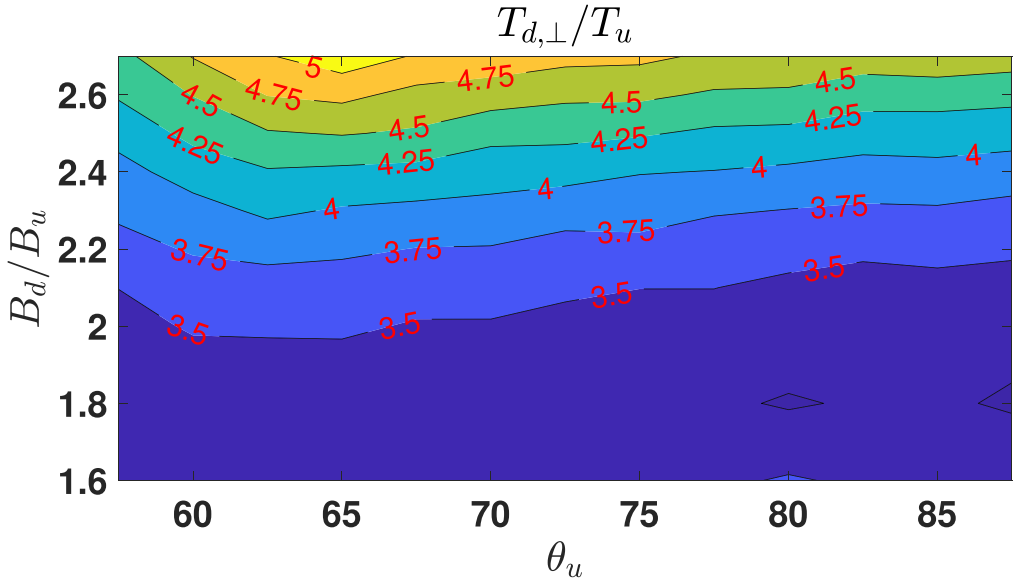


**Figure 6.** Perpendicular heating $T_{d,\perp}/T_u$ as a function of $B_d/B_u$ and $\theta_u$.

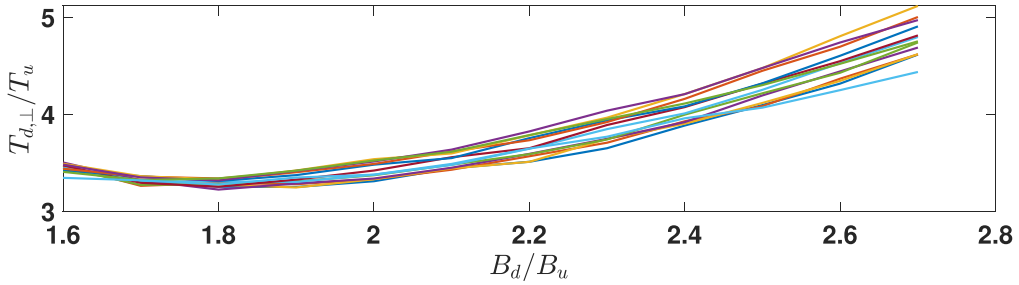


**Figure 7.** Perpendicular heating $T_{d,\perp}/T_u$ as a function of $B_d/B_u$ for different $\theta_u$.

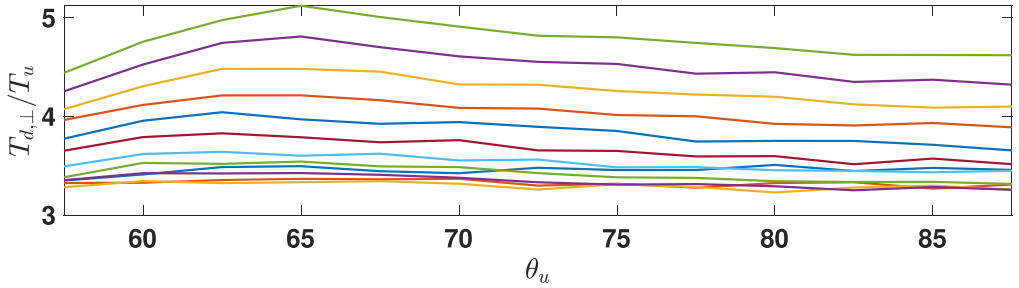


**Figure 8.** Perpendicular heating $T_{d,\perp}/T_u$ as a function of $\theta_u$ for different $B_d/B_u$. At the high end of $\theta_u$ larger values of $T_{d,\perp}/T_u$ correspond to larger $B_d/B_u$.

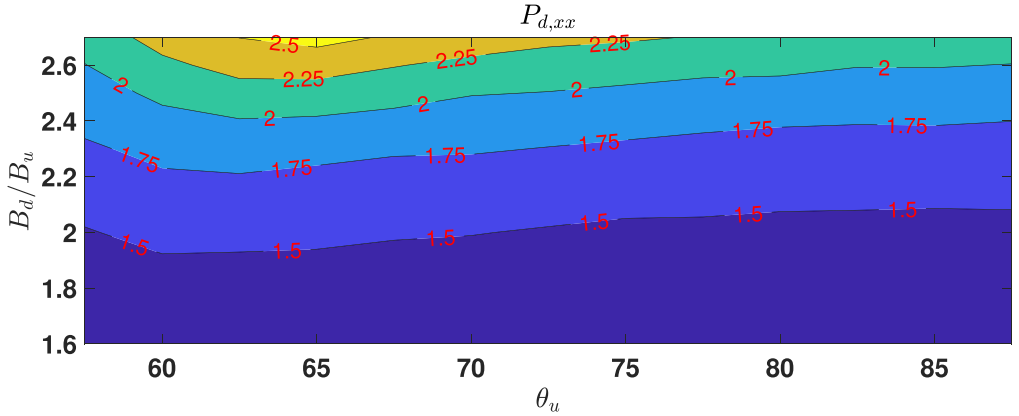


**Figure 9.** The downstream pressure $P_{d,xx}$ as a function of $B_d/B_u$ and $\theta_u$.

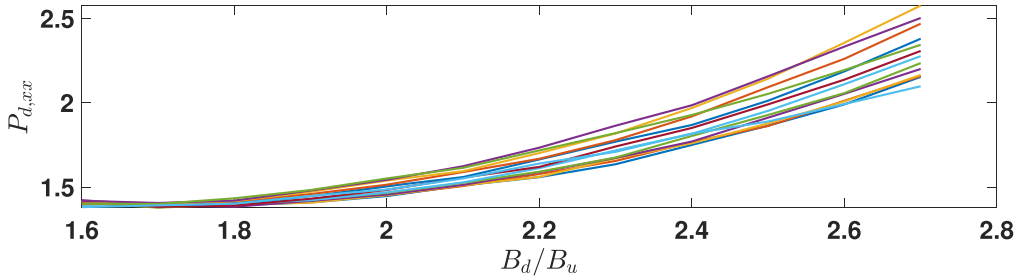


**Figure 10.** The downstream pressure $P_{d,xx}$ as a function of $B_d/B_u$ for various $\theta_u$.

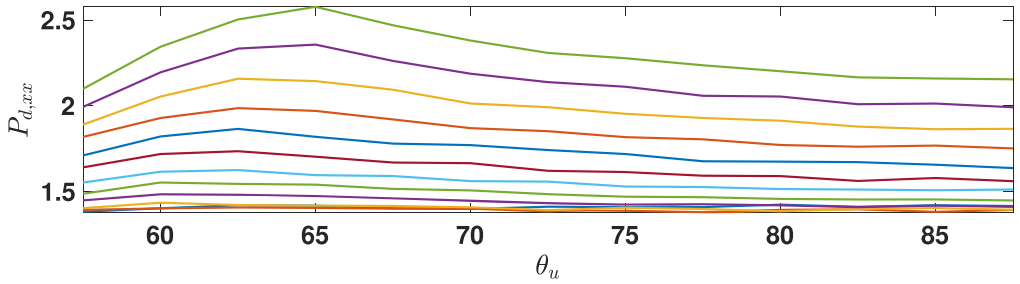


**Figure 11.** The downstream pressure $P_{d,xx}$ as a function of $\theta_u$ for various $B_d/B_u$.

## 4. Estimate of Heating at the Termination Shock

The pressure balance reads

$$n_u m_p V_u^2 + P_{u,\mathrm{PUI}} + P_{u,\mathrm{SW}} + P_{u,e} + \frac{B_u^2}{8\pi} = n_d m_p V_d^2 + P_{d,\mathrm{PUI}} + P_{d,\mathrm{SW}} + P_{d,e} + \frac{B_d^2}{8\pi}. \quad (14)$$

The kinetic pressure of the solar wind and electrons in the upstream region can be neglected. Typical electron heating values (Schwartz et al. 1988) are much smaller than the SW proton heating, so that the downstream electron pressure is a small correction beyond the precision of the analysis. Thus, the appropriate approximation reads

$$P_{d,\mathrm{PUI}} = \frac{2}{3}P_{d\perp,\mathrm{PUI}} + \frac{1}{3}P_{d\parallel,\mathrm{PUI}} = n_{d,\mathrm{PUI}}T_{d,\mathrm{PUI}} \quad (15)$$

$$P_{d,\mathrm{sw}} = n_{d,\mathrm{SW}}T_{d,\mathrm{SW}}. \quad (16)$$

Let $\xi = n_{u,\mathrm{PUI}}/n_u$, where $n_u = n_{u,\mathrm{SW}} + n_{u,\mathrm{PUI}}$ then the pressure balance will take the form

$$1 + \xi\frac{T_{u,\mathrm{PUI}}}{m_p V_u^2} + \frac{1}{2M^2} = \frac{1}{R_d} + R_d\xi\frac{T_{d,\mathrm{PUI}}}{m_p V_u^2} + R_d(1-\xi)\frac{T_{d,\mathrm{SW}}}{m_p V_u^2} + \frac{R^2}{2M^2}, \quad (17)$$

where we used the approximation that the density compression $R_d = n_d/n_u$ is the same for all species. Using $\xi = 0.2$, $R_d = 2.7$, $R = 2.5$, $M = 6.5$, $T_{u,\mathrm{PUI}}/m_p V_u^2 = 0.14$, and $R_d T_{d,\mathrm{PUI}}/m_p V_u^2 = 1.2/2.7$ one finds $T_{d,\mathrm{SW}}/m_p V_u^2 \approx 0.18$. In absolute units, we have for $V_u = 300\,\mathrm{km\,s^{-1}}$:

$$T_{d,\mathrm{PUI}} \approx 6.6 \times 10^6\ \mathrm{K},\ T_{d,\mathrm{SW}} \approx 1.0 \times 10^6\ \mathrm{K},\ T_d = 2.1 \times 10^6\ \mathrm{K}, \quad (18)$$

where we introduced the mean downstream temperature of the mixture $T_d = (P_{d,\mathrm{SW}} + P_{d,\mathrm{PUI}})/n_d$ (Zank et al. 2010). The *relative* SW heating $T_{d,\mathrm{SW}}/T_{u,\mathrm{SW}}$ is much *larger* than the *relative* PUI heating $T_{d,\mathrm{PUI}}/T_{u,\mathrm{PUI}}$. The *absolute* SW heating $T_{d,\mathrm{SW}} - T_{u,\mathrm{SW}}$ is much *smaller* than the *absolute* PUI heating $T_{d,\mathrm{PUI}} - T_{u,\mathrm{PUI}}$. For $V_u = 200\,\mathrm{km\,s^{-1}}$ (Richardson 2008; Richardson et al. 2008) one gets

$$T_{d,\mathrm{PUI}} \approx 2.9 \times 10^6\ \mathrm{K},\ T_{d,\mathrm{SW}} \approx 4.6 \times 10^5\ \mathrm{K},\ T_d = 9.6 \times 10^5\ \mathrm{K}. \quad (19)$$

An increase of the PUI fraction to $\xi = 0.3$ (Ariad & Gedalin 2013) with $V_u = 200\,\mathrm{km\,s^{-1}}$ gives

$$T_{d,\mathrm{PUI}} \approx 2.9 \times 10^6\ \mathrm{K},\ T_{d,\mathrm{SW}} \approx 1.4 \times 10^5\ \mathrm{K},\ T_d = 9.8 \times 10^5\ \mathrm{K}. \quad (20)$$

Note the strong dependence of the SW temperature on the fraction of PUI. For comparison, for $\xi = 0.05$ and $V_u = 200\,\mathrm{km\,s^{-1}}$ the relation (17) would give $T_{d,\mathrm{SW}} \approx 8 \times 10^5\,\mathrm{K}$. The mean downstream temperature varies weakly and remains on the order of $10^6$ K.

## 5. Particle-in-cell Simulations

Particle tracing calculations are performed using simplifying assumptions regarding the profile of magnetic field and the cross-shock potential. It is therefore desirable to compare the predictions obtained with self-consistent shock simulations, where the PUI dynamics and shock structure are mutually dependent. We have performed a series of 1D particle-in-cell (PIC) simulations with varying upstream conditions, such as the upstream fraction of PUI, shock speed, and shock angle $\theta_u$. The shock is formed using reflection from a wall located at the origin. The upstream plasma is continuously injected at the opposite boundary of the simulation domain. Upstream plasma is assumed to consist of electrons with an isotropic Maxwellian distribution with density $n_0$ and temperature $T_e$, PUIs with a filled-shell distribution (Vasyliunas & Siscoe 1976) with density $n_{\mathrm{PUI}}$ and cutoff speed $U_{\mathrm{PUI}}^c$, and solar wind protons with an isotropic Maxwellian distribution with density $n_{\mathrm{SW}} = n_0 - n_{\mathrm{PUI}}$ and temperature $T_{\mathrm{SW}} = T_e$. The three

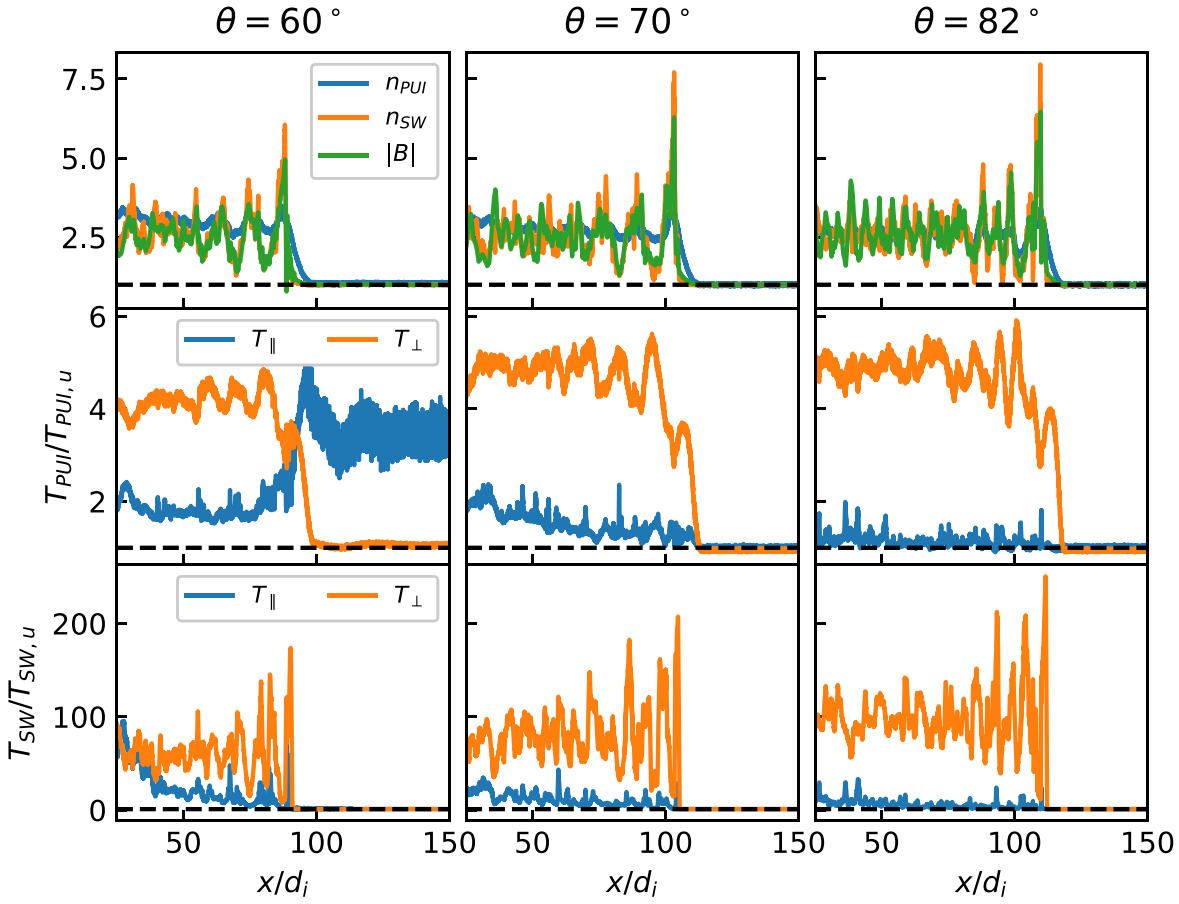


**Figure 12.** Indicative results of PIC simulations for three different angles.

simulations chosen for presentation here are identical with the exception of the shock angle. The upstream electron $\beta_e = 8\pi n_o T_e/B_0^2 = 0.1$, the PUI fraction is $n_{\rm PUI}/n_0 = 0.2$, the cutoff speed is $U^c_{\rm PUI} = 7V_{\rm A}$ (corresponding approximately to the shock speed, see below), the domain length is $L_x = 200d_i$, the number of cells is approximately $1.8\times10^5$, corresponding to approximately resolution of approximately one Debye lengths. The ratio of upstream plasma frequency to electron cyclotron frequency is $\omega_{pe}/\Omega_{ce} = 10$ and mass ratio $m_i/m_e = 400$. Here $d_i = c/\omega_{pi}$ is the proton inertial length, $\omega_{p\alpha} = 4\pi n_0 e^2/m_\alpha^{1/2}$, and $m_\alpha$ is the mass of species $\alpha$. The simulations were performed using the VPIC code (Bowers et al. 2008).

Figure 12 shows a summary of the simulations performed with $\theta_u = 60°$, $\theta_u = 70°$, and $\theta_u = 82°$. For each angle, the top rows show the profiles of magnetic field, solar wind proton density, and PUI density. While all the simulations have the same injection speed, the shock speed with respect to the simulation frame varies slightly, resulting in slightly different total shock speed for three cases, $M_{\rm A} = (6.7,\ 7,\ 7.2)V_{\rm A}$ for $\theta_u = 60°,\ 70°,\ 82°$, respectively. The compression ratio is similar in all three cases: $B_d/B_u \approx 2.5$, where $B_d$ is averaged over the downstream wavetrain. For lower angles, the PUI density increase immediately behind the shock ramp is slightly higher than that of the solar wind protons and that of the magnetic field, but eventually it approaches the same value at a distance of the order of $100d_i$. The second and third rows in Figure 12 show the parallel and perpendicular (with respect to the local magnetic field) temperatures of PUIs and solar wind protons, respectively. The temperature is defined as the second moment of the distribution. The large increase in the upstream PUI temperature at $\theta = 60°$ is due to backstreaming PUIs, which are not present at larger angles. The ratio of downstream to upstream $T_\perp$ increases slightly with shock angle and shock speed, from approximately 4.2 at $\theta = 60°$ and $M_{\rm A} = 6.7$ to approximately 5 at $\theta_u = 82°$ and $M_{\rm A} = 7.2$. The relative increase of solar wind proton temperature is much higher that that of the PUIs, although the downstream PUI temperature is still significantly higher than that of SW protons.

## 6. Conclusions

In the present paper we have found, for the first time, the downstream gyrotropic distributions of PUI for a variety of the shock magnetic compressions and shock angles in the quasi-perpendicular regime. The analysis provides the downstream perpendicular and parallel temperatures, and the downstream density. The temperature of the isotropic distribution at the MHD scale can be obtained as $T = (2/3)T_\perp + (1/3)T_\parallel$. The results can be used in the jump conditions at the termination shock, while the upstream PUI-to-solar wind density ratio is a free adjustable parameter. Here we restricted ourselves only with the analysis of the dependence of the downstream PUI distributions on the major shock parameters. The expected SW heating was estimated using the total pressure balance and the obtained PUI heating. Obviously, shock heating of the solar wind does not depend on PUIs. However, SW heating is more sensitive to as yet unknown fine structure of the shock front. Therefore, here we avoided studying SW heating in our test particle analysis.

This research was partially supported by NASA grant 80NSSC18K1649, and NSF-BSF grants 2010144 and 2010450. N.P. was also supported by the IBEX mission as a part of NASA's Explorer program. The authors acknowledge the Texas Advanced Computing Center (TACC) at The University of Texas at Austin for providing HPC resources on Frontera supported by NSF LRAC award 2031611, which have contributed to the research results reported within this paper. PIC simulations were partly performed using resources provided by the NASA High-End Computing (HEC) Program through the NASA Advanced Supercomputing (NAS) Division at Ames Research Center. M.G. was partially supported by NSF-BSF grant 2019744. A table with the results of the analysis is published at https://doi.org/10.7910/DVN/CVOZGO. The table presents $P_{d,xx}$, $T_{d,\perp}$, and $n_d/n_u$ for 156 combinations of $B_d/B_u$ and $\theta_u$.

## ORCID iDs

Michael Gedalin https://orcid.org/0000-0003-1236-4787
Nikolai V. Pogorelov https://orcid.org/0000-0002-6409-2392
Vadim Roytershteyn https://orcid.org/0000-0003-1745-7587

## References

Ariad, D., & Gedalin, M. 2013, JGR, 118, 2854
Borovikov, S. N., Pogorelov, N. V., Burlaga, L. F., & Richardson, J. D. 2011, ApJL, 728, L21
Bowers, K. J., Albright, B. J., Yin, L., Bergen, B., & Kwan, T. J. T. 2008, PhPl, 15, 055703
Burlaga, L. F., Ness, N. F., Acuña, M. H., et al. 2008, Natur, 454, 75
Burrows, R. H., Zank, G. P., Webb, G. M., Burlaga, L. F., & Ness, N. F. 2010, ApJ, 715, 1109
Drury, L. O. 1983, RPPh, 46, 973
Fahr, H. J., & Chalov, S. V. 2008, A&A, 490, L35
Fahr, H. J., & Siewert, M. 2013, A&A, 558, A41
Fahr, H. J., & Siewert, M. 2015, A&A, 576, A100
Fahr, H. J., Siewert, M., & Chashei, I. 2012, Ap&SS, 341, 265
Florinski, V., Decker, R. B., Le Roux, J. A., & Zank, G. P. 2009, GeoRL, 36, 12101
Gedalin, M. 1996, JGR, 101, 4871
Gedalin, M. 2016a, PhPl, 23, 102904
Gedalin, M. 2016b, JGR, 121, 10
Gedalin, M. 2017, JGR, 122, 11
Gedalin, M. 2020, PhRvE, 102, 1
Gedalin, M., & Balikhin, M. 2008, JPlPh, 74, 207
Gedalin, M., Pogorelov, N. V., & Roytershteyn, V. 2020, ApJ, 889, 116
Jokipii, J. R. 2013, SSRv, 176, 115
Kennel, C. F. 1994, in AIP Conf. Proc. 314, Advances in Plasma Physics, The Magnetohydrodynamic Rankine–Hugoniot Relations (Melville, NY: AIP), 180
Kumar, R., Zirnstein, E. J., & Spitkovsky, A. 2018, ApJ, 860, 156
Lee, M. A., Shapiro, V. D., & Sagdeev, R. Z. 1996, JGR, 101, 4777
Li, H., Wang, C., & Richardson, J. D. 2008, GeoRL, 35, 19107
Lyu, L. H., & Kan, J. R. 1986, JGR, 91, 6771
Matsukiyo, S., & Scholer, M. 2011, JGR, 116, 08106
Matsukiyo, S., & Scholer, M. 2014, JGR, 119, 2388
Mostafavi, P., Zank, G. P., & Webb, G. M. 2016, in AIP Conf. Proc. 1720, Solar Wind 14 (Melville, NY: AIP), 1
Mostafavi, P., Zank, G. P., & Webb, G. M. 2017, JPhCS, 900, 012016
Mostafavi, P., Zank, G. P., & Webb, G. M. 2018, JGR, 868, 120
Pogorelov, N. V., Borovikov, S. N., Bedford, M. C., et al. 2013, in ASP Conf. Ser. 474, Numerical Modeling OfSpace Plasma Flows (San Francisco, CA: ASP), 165
Richardson, J. D. 2008, GeoRL, 35, L23104
Richardson, J. D., Kasper, J. C., Wang, C., Belcher, J. W., & Lazarus, A. J. 2008, Natur, 454, 63
Schwartz, S. J., Thomsen, M. F., Bame, S. J., & Stansberry, J. 1988, JGR, 93, 12923
Terasawa, T. 1979, P&SS, 27, 193
Toptyghin, I. N. 1980, SSRv, 26, 157
Vasyliunas, V. M., & Siscoe, G. L. 1976, JGR, 81, 1247
Zank, G. P. 2016, GSL, 3, 22
Zank, G. P., Heerikhuisen, J., Pogorelov, N. V., Burrows, R., & McComas, D. 2010, ApJ, 708, 1092
Zank, G. P., Hunana, P., Mostafavi, P., & Goldstein, M. L. 2014, ApJ, 797, 87
Zank, G. P., Pauls, H. L., Cairns, I. H., & Webb, G. M. 1996, JGR, 101, 457
Zilbersher, D., & Gedalin, M. 1997, P&SS, 45, 693